Intraoperative 3D reconstruction and geometric modeling using sensorized microsurgical instruments

Marius Briel, Ludwig Haide, Jule Emmrich, Nicola Piccinelli, Gernot Kronreif, Eleonora Tagliabue and Franziska Mathis-Ullrich

***Abstract*—Precise micrometer-scale tissue manipulation is essential for successful microsurgery. Despite advancements in intraoperative sensing and instrument tracking, providing accurate real-time feedback on instrument positions relative to critical tissue structures remains challenging. This research aims to reliably reconstruct fine-grained anatomical surfaces intraoperatively using a smart instrument with fiber-based distance sensing. First, instrument-integrated optical coherence tomography sensor readings are integrated with instrument tracking to reconstruct accurate surface point clouds. Subsequently, radial basis functions, ordinary Kriging, and B-splines are utilized for surface modeling, employing tailored basis functions and smoothing parameters. The proposed methods are validated in the context of vitreoretinal surgery through simulations and with ex vivo studies involving porcine and human cadaver eyes. In simulations, radial basis function interpolation demonstrates the highest robustness across varying noise levels and eye shapes. In ex vivo studies, ordinary Kriging outperformed, yielding root mean square errors of $14.7\,\mu\text{m}$ for the porcine eye and $38.1\,\mu\text{m}$ for the human eye, with $99.7\,\%$ and $96.5\,\%$ of absolute errors below $100\,\mu\text{m}$. The proposed methods effectively model feature-rich micro-anatomical surfaces and enable model-based assistance and automation, ultimately enhancing surgical precision in delicate ophthalmic procedures.**

***Index Terms*—Intraoperative anatomical models, microsurgery, optical coherence tomography, intraoperative guidance**

I. Introduction

FOR many patients with severe disease, challenging surgery on fragile, micron-scale tissue is essential. Due to the limited visibility and challenging lighting conditions, feedback on the surgical instrument's position relative to the tissue can significantly assist surgeons [1]. This necessity drives the development of smart microsurgical instruments equipped with real-time distance sensing capabilities, alongside instrument tracking algorithms. These innovations facilitate the intraoperative three-dimensional reconstruction of tissue surfaces (Fig. 1).

Manuscript created: Month, Year; revised Month, Day, Year; accepted Month, Day, Year. This work was supported by the European Union's Horizon Europe research and innovation programme under grant agreement N° 101070443. GEYEDANCE: AI Guidance for Robot-Assisted Eye Surgery (https://geyedance.eu).

Marius Briel, Ludwig Haide, Eleonora Tagliabue are with Carl Zeiss AG, 73447 Oberkochen, Germany (e-mail: marius.briel@zeiss.com)

Franziska Mathis-Ullrich, Marius Briel are with Surgical Planning and Robotic Cognition Laboratory (SPARC), Friedrich-Alexander-University Erlangen-Nürnberg, Germany (e-mail: franziska.mathis-ullrich@fau.de)

Jule Emmrich is with Karlsruhe Institute of Technology, Germany

Nicola Piccinelli is with Department of Engineering for Innovation Medicine, Università di Verona, Italy (e-mail: nicola.piccinelli@univr.it)

Gernot Kronreif is with Austrian Center for Medical Innovation and Technology, Wiener Neustadt, Austria (e-mail: gernot.kronreif@acmit.at)

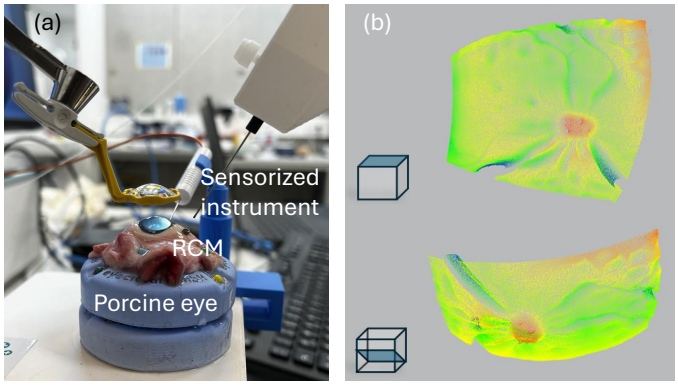

Fig. 1: (a) An optical sensor integrated with a remote center of motion (RCM)-constrained instrument measures the distance from the instrument tip to the tissue. (b) This enables the reconstruction of small surface irregularities in a porcine retina, such as retinal folds near the optic disc, within the robot's base frame. The blue view planes within the cubes illustrate the viewing direction

Optical fibers have been incorporated into various medical instruments, including needles [2], forceps [3], and vitrectomy cutters [4], facilitating tomographic imaging from within the body, such as in neurosurgery [5]. The clinical application of instrument-integrated optical coherence tomography (iiOCT) distance sensors in robotic vitreoretinal surgery was first demonstrated by Cereda et al. [6]. Alternatively, a sensorized instrument that uses projection patterns from an integrated spotlight analyzed through a microscope camera offers a cost-effective but less accurate means of intra-ocular distance measurement [7].

In this paper, we focus on vitreoretinal surgery as a representative application due to its significance in microsurgery and the high volume of procedures performed [8]. Intraoperative optical coherence tomography (OCT) volume imaging is primarily used for instrument tracking in ophthalmic surgery, often in conjunction with surgical microscopes [9]–[11]. Alternatively, real-time pose tracking can be achieved through electromagnetic tracking systems, such as the Aurora system (NDI, Waterloo, Canada), or through robotics. Closed-loop telemanipulators such as the hybrid parallel-serial micromanipulator developed by Nasseri et al. [12] are capable of tracking joint movements, and with forward kinematics, the instrument pose in the world reference frame can be retrieved, provided the instrument is extrinsically calibrated to the robot. Piccinelli et al. introduced the Geyedance system [13],

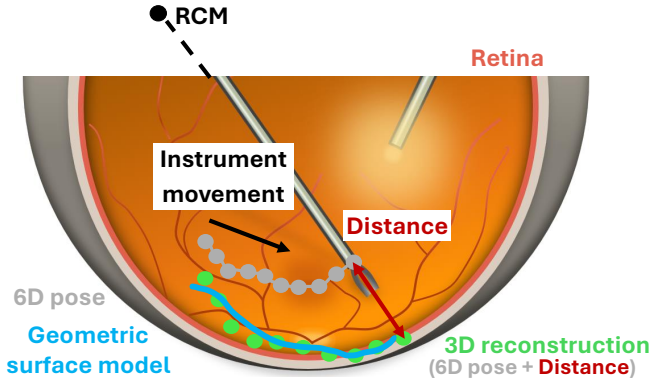

Fig. 2: Intraoperative reconstruction of the 3D retinal point cloud is achieved by combining distance measurements with the 6D tool tip pose during instrument movement. The reconstructed point cloud is used for patient-specific geometric modeling

a bilateral teleoperated microsurgery platform with OCT-measurement integrated at the end-effector, providing multimodal feedback. The system exploits a neural network-based tool-to-tissue distance estimation module to enable surface reconstruction and intraoperative spherical modeling.

Intraoperative eye modeling utilizing extra-ocular sensors presents significant challenges due to optical distortions originating from the anterior segment of the eye [14]. Additionally, microscope-based surface reconstruction is hindered by difficulties in depth reconstruction [15], [16]. Initial research on eye modeling utilizing intra-ocular sensors, such as iiOCT or endoscopy, has focused on approximating the eye with spherical fits [17], [18]. Briel et al. demonstrated that ellipsoid fitting is superior to sphere fitting for regular eye shapes [19]. However, in real-world experiments, neither model achieves errors below $100\,\mu\mathrm{m}$, highlighting the need for more flexible surface modeling methods able to account for local structures such as blood vessels, bumps, puckers, and the optic nerve head (ONH).

In this work, we propose a patient-specific geometrical modeling method that utilizes only intraoperative point clouds from instrument-integrated measurements, eliminating the need for preoperative-intraoperative registration [20] or generic model assumptions [19]. The high precision of the 3D reconstruction is validated in ex vivo studies on porcine and human cadaver eyes through comparison with microscope images and microscope-integrated OCT. The model's accuracy, enhanced by techniques such as smoothing parameter optimization, is further demonstrated by comparison with a 3D reference point cloud.

II. Method

Instrument-integrated OCT measurements are combined with instrument tracking to reconstruct accurate surface point clouds, following the reconstruction method proposed in [13] and illustrated in Fig. 2. We propose teleoperated surface exploration instead of automated movements, enabling surgeons to target regions of high relevance. Subsequently, we present patient-specific geometrical modeling techniques. Unlike previous methods, our modeling approaches do not enforce any predefined geometric shapes (e.g., sphere or ellipsoid) while preserving smoothness and retaining critical retinal features. We present radial basis functions [21], ordinary Kriging [22], and B-splines [23], which are particularly effective for precise and flexible retinal modeling due to their successful application in related research fields [24], [25].

A. Intraoperative 3D reconstruction

iiOCT conducts one-dimensional intensity scans, known as A-scans, of reflections from structures such as the retina. This technique enables visualization of the retinal surface and the layers beneath it. Convolutional neural networks can be employed for real-time segmentation of retinal layers in A-scans, enabling the estimation of the distance from the instrument tip to the retinal surface [26]. To prevent segmentation errors, we manually annotated the time-resolved A-scans, referred to as M-scans. Adding a temporal dimension to the A-scans simplifies the annotation process, allowing annotators with limited clinical background to successfully perform the task. In previous work [13], we showed that our U-Net-like convolutional network achieves mean absolute distance errors of $14\,\mu\mathrm{m}$ when trained on simulated iiOCT data from microscope-integrated OCT and tested on cadaver eye data. When trained on cadaver eye data, the error decreases to $7\,\mu\mathrm{m}$.

By using forward kinematics to determine the pose of the surgical instrument, the measured distance can be converted into a spatial point on the surface, following the approach outlined in [13]. Moving the smart instrument and collecting data points generates a point cloud that represents the surface (Fig. 2). In this work, we propose teleoperated surface exploration to allow surgeons to target areas with surface anomalies or regions of high relevance, thereby reducing reconstruction errors in these regions. In contrast, our previous work introduced an automated spiral trajectory for pre-surgery exploration [19]. Teleoperated exploration provides surgeons with full control of the instrument, allowing them to delineate the surgical area and define the model's scope.

Intraoperative models must address the noise and non-uniformity characteristics inherent in the reconstructed point clouds. These challenges stem from difficulties in estimating distances using A-scans and inaccuracies in tracking the instrument tip, often caused by movement constraints imposed by the remote center of motion (RCM) or calibration issues.

B. Radial basis functions

The radial basis function (RBF) interpolation method is a robust global approach that utilizes all available data points for modeling [21]. Given a set of data points $\{x_i\}_{i=1}^n$ with corresponding values $\{z_i\}_{i=1}^n$, our goal is to find the interpolant $z = s(x)$ for all points x in the ocular region of interest. In this context, $\{x_i\}_{i=1}^n$ represents the lateral 2D coordinates (x and y) of the reconstructed point cloud in the robot base frame, while $\{z_i\}_{i=1}^n$ denotes the z-coordinates. The z-axis aligns with the instrument axis in the robot's initial configuration, which is angled at 30° to the world upward

direction. RBF interpolation effectively manages unevenly scattered data across multiple dimensions [27] by employing a linearly weighted sum of radially symmetric basis functions ϕ centered at the data points x_i:

$$s(x) = \sum_{i=1}^{n} \alpha_i \phi(\|x - x_i\|) + \sum_{j=0}^{m} \beta_j p_j(x)\,, \tag{1}$$

where α_i and β_j are the unknown interpolant coefficients and p_j polynomials in x. This approach enables local z-value approximation, making it suitable for modeling complex, smooth surfaces with a minimal pointwise error [28].

The radial basis functions (i.e., kernels) must be conditionally positive definite to ensure the solvability and uniqueness of the following linear equation system [27]:

$$\begin{pmatrix} \Phi & P \\ P^T & 0 \end{pmatrix} \begin{pmatrix} \boldsymbol{\alpha} \\ \boldsymbol{\beta} \end{pmatrix} = \begin{pmatrix} \mathbf{z} \\ \mathbf{0} \end{pmatrix}, \tag{2}$$

where $\Phi \in \mathbb{R}^{n\times n}$ is the RBF matrix and $P \in \mathbb{R}^{n\times(m+1)}$ is the polynomial matrix, $\boldsymbol{\alpha} \in \mathbb{R}^n$ are the RBF coefficients, and $\boldsymbol{\beta} \in \mathbb{R}^{m+1}$ are the polynomial coefficients.

A key advantage of RBF interpolation is its capacity to smooth irregularities and noise in measured data. To address noise in the input data of the RBF interpolator, a smoothing parameter $\lambda \geq 0$ is introduced, modifying the system to

$$\begin{pmatrix} \Phi + \lambda I & P \\ P^T & 0 \end{pmatrix} \begin{pmatrix} \boldsymbol{\alpha} \\ \boldsymbol{\beta} \end{pmatrix} = \begin{pmatrix} \mathbf{z} \\ \mathbf{0} \end{pmatrix}, \tag{3}$$

where I is the identity matrix. The calculation of the coefficients α_i thus becomes a balance between accurately fitting the data and allowing some flexibility to smooth out noise.

C. Ordinary Kriging

Ordinary Kriging (OK) is an interpolation technique initially developed in geostatistics [22] and has since then been applied in areas like three-dimensional optical surface metrology [29]. It is based on the principle that spatially close points tend to have similar values, utilizing a stochastic model to capture these spatial dependencies. Regionalized variable theory addresses this by treating z-values as stochastic variables $z(x)$ rather than deterministic ones. Key assumptions of this theory include an unknown but constant mean, stationary variance and isotropy [22].

The expected squared difference between values at two points separated by a lag h is described by the semivariance $\gamma(h)$

$$2\gamma(h) := \mathbb{E}[(z(x) - z(x+h))^2]\,. \tag{4}$$

The function that relates the semi-variance $\gamma(h)$ to the separation vector h is known as the variogram. To capture spatial autocorrelation in the data, the empirical variogram is defined as

$$\hat{\gamma}(h) = \frac{1}{2M(h)} \sum_{i=1}^{M(h)} \left(z(x_i) - z(x_i + h)\right)^2, \tag{5}$$

where $M(h)$ describes the number of pairs of observations $z(x_i)$ and $z(x_i + h)$ separated by the lag h. The precision of the estimated semivariances depends on the sample sizes $M(h)$ [22]. After evaluating the empirical variogram for various lags h, a spherical experimental variogram model is fitted through the semivariances.

The variogram model characterizes correlation properties of data points through the *range*, *sill*, and *nugget* value. The *range* indicates the lag beyond which data points are deemed uncorrelated, whereas the *sill* represents the plateau value attained at maximum range. The *nugget* accounts for variability among data points at very short distances (i.e., noise) and is where the variogram intersects the y-axis.

The prediction at an unobserved location is calculated as a weighted sum of observed data points [30]:

$$\hat{z}(x) = \sum_{i=1}^{n} \alpha_i z(x_i)\,, \tag{6}$$

where $\alpha_i \in \mathbb{R}$ are the OK coefficients optimized for prediction. The best linear unbiased ($\sum_i \alpha_i = 1$) predictor is found by minimizing the variance of the interpolation error, leading to the following equation system

$$\begin{bmatrix} \Gamma & \mathbf{1} \\ \mathbf{1}^T & 0 \end{bmatrix} \begin{bmatrix} \boldsymbol{\alpha} \\ \mu \end{bmatrix} = \begin{bmatrix} \boldsymbol{\gamma} \\ 1 \end{bmatrix}, \tag{7}$$

where $\Gamma \in \mathbb{R}^{n\times n}$ is the matrix of semivariances, $\boldsymbol{\gamma} \in \mathbb{R}^n$ is the vector of semivariances between the unobserved location x and the known locations x_i, and μ represents the Lagrange parameter. OK uncertainty enables the assessment of the reliability of interpolated values based on variances.

D. B-splines

Basis spline surface reconstruction is a versatile technique to create smooth surfaces that are defined by a control lattice. Adjustments to a control point affect only a specific region of the surface, enhancing computational efficiency and making it valuable in computer graphics and CAD applications [23]. Dewan et al. utilize third-order tensor B-splines to model disparities in stereo images, achieving a 3D reconstruction that guides the user along the surface [31]. The degree of the B-spline determines the surface's smoothness with cubic B-splines frequently used for their balance of flexibility and smoothness.

A B-spline surface is defined as a tensor product of B-spline basis functions along each parameter direction, consisting of continuous surface patches that connect seamlessly at their boundaries and possess continuous higher-order derivatives. The general formula for a B-spline surface is

$$f(u,v) = \sum_{i=0}^{m} \sum_{j=0}^{n} \mathbf{P}_{i,j} N_i^k(u) N_j^l(v)\,, \tag{8}$$

where u and v are the global parameters of the surface patch, $P_{i,j}$ are the control points, and $N_i^k(u)$ and $N_j^l(v)$ are the B-spline basis functions.

To obtain the spline surface, the following function is minimized:

$$F = \sum_i \omega_i \cdot (z_i - f(u_i, v_i))^2 + \lambda \int \left(\left(\frac{\partial^2 f}{\partial u^2}\right)^2 + \left(\frac{\partial^2 f}{\partial v^2}\right)^2 + 2\left(\frac{\partial^2 f}{\partial u\,\partial v}\right)^2 \right) du\,dv\,. \tag{9}$$

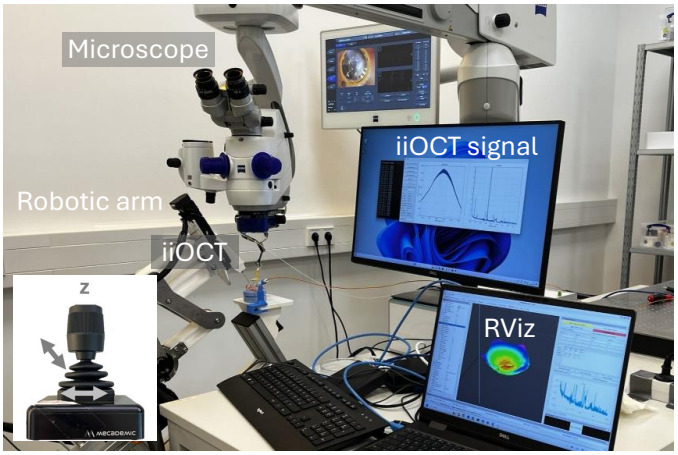

Fig. 3: The robotic system including a 3 DOF telemanipulator and iiOCT sensing [13] performs measurements on a porcine eye visualized under a surgical microscope

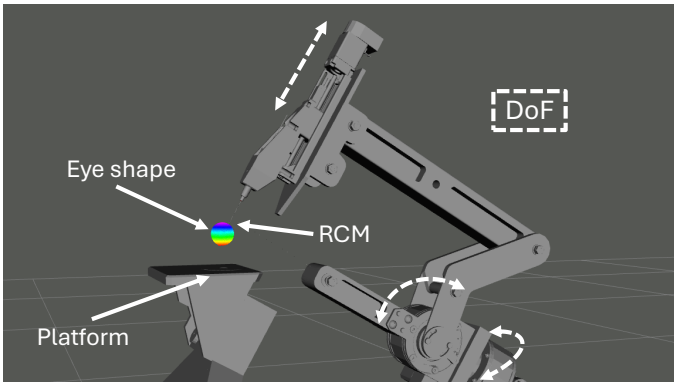

Fig. 4: Visualization of the three-degree-of-freedom Geyedance robotic system in RViz [13], featuring a mechanical RCM. Simulated distance measurements between the virtual instrument tip and eye shape are possible

The first term represents the approximation quality of $f(u, v)$ at the data points (u_i, v_i, z_i), whereas the penalty term measures the spline's bending energy, a common smoothing approach [32]. The parameter λ balances smoothing and fidelity to the data. Minimizing F is achieved by adjusting the positions of the control points.

III. Experimental Validation

A. Experimental setup

The experimental setup (Fig. 3) integrates the Geyedance robotic system and optical-fiber-based instrument-integrated sensing [13]. The robotic system is interfaced and controlled using Robot Operating System (ROS) and teleoperated via a TCP connection with the MJ3 joystick (Mecademic, Montreal, Canada). In ROS, the system simulation includes a robot model controllable with the MJ3 joystick and simulated instrument-retina distance measurements (Fig. 4).

The customized robotic arm (ACMIT, Wiener Neustadt, Austria), a three-degree-of-freedom manipulator, features a parallel kinematic structure that provides a mechanical RCM.

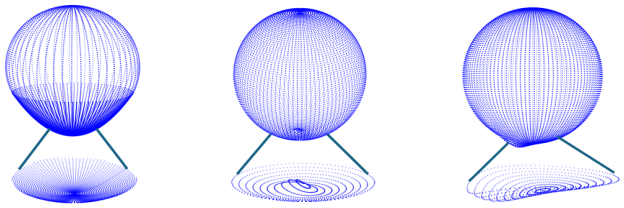

Fig. 5: Ground truth point clouds of the pointed retina, retinal detachment, and staphyloma with their local modeling areas

With the RCM as a movement constraint, defining the angle between the instrument and the retina, it allows a pivoting range of +/- 40° for both rotating axes around the RCM and a linear instrument insertion with a range of $10\,\mathrm{cm}$. The manipulator is controlled using an MJ3 joystick, a 3-axes joystick suitable for operating the robot in joint velocity mode. The linear guide includes an instrument holder for inserting the iiOCT cannula to perform intra-ocular distance measurements.

The common-path OCT provided by ACMIT (Wiener Neustadt, Austria) achieves $12\,\mathrm{mm}$ imaging depth and a resolution of $23.4\,\mu\mathrm{m}$. The surgical microscope is used to observe and monitor the surgical field and includes a microscope-integrated OCT used as a reference modality to assess the quality of the 3D reconstruction. The OCT-scan consists of 512×128 A-scans, each containing 1024 pixels, with an imaging depth of $2.9\,\mathrm{mm}$ in tissue. Its size is adjusted to align with the scanned area of the iiOCT.

B. Data acquisition in simulation

Three distinct eye shapes [19] are constructed as point clouds based on parameters from the literature [33], [34] and illustrated in Fig. 5. These eye shapes represent common pathological conditions, including staphyloma, retinal detachment and pointed retina. A staphyloma is characterized by a localized protrusion at the posterior part of the eye, while retinal detachment occurs when the retina tears, allowing vitreous fluid to seep into the subretinal space. Nearly half of highly myopic eyes exhibit a pointed shape in the posterior part [35]. By incorporating a point cloud of a designed eye shape, simulated distances to the eye surface are measured in the instrument direction. This is achieved by calculating the intersection with the plane fitted through the closest points to the iiOCT ray.

To identify the most reliable local modeling method and its optimal parameters, experiments are initially conducted in simulation. To assess the minimal time needed for reliable reconstruction, nested trajectories with durations of $30\,\mathrm{s}$, $45\,\mathrm{s}$, $60\,\mathrm{s}$, $90\,\mathrm{s}$, $120\,\mathrm{s}$ are acquired, covering a circular area of approximately $4\,\mathrm{mm}$ radius. The robotically-held surgical instrument is maneuvered in RViz for $2\,\mathrm{min}$ using a joystick, continuously acquiring simulated distance measurements and storing the trajectories at the specified time stamps. The authors, without clinical backgrounds, collected a total of five distinct trajectories for each eye shape while monitoring the measured points in real-time within the RViz simulation

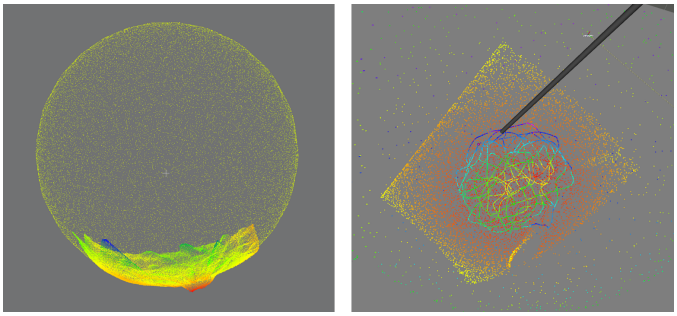

Fig. 6: Acquisition of realistic exploration data in RViz (right) derived from a real-world grid scan of a porcine retina (left)

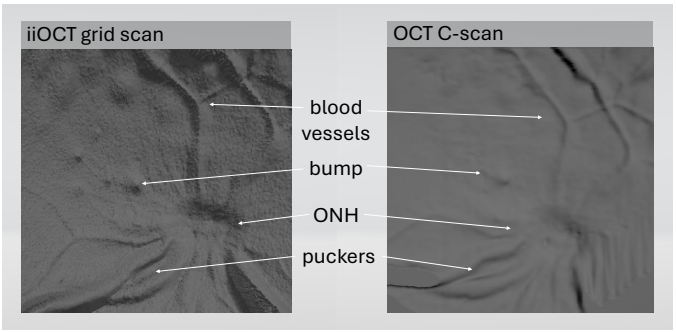

Fig. 7: Comparision of surface characteristics in the meshed iiOCT grid scan and the OCT volume scan of the porcine eye

environment. The trajectories are designed to evenly scan the entire region of interest, specifically the macular area, with an emphasis on surface irregularities.

C. Ex vivo data acquisition

Further, a human cadaver eye study was conducted at Ospedale Privato Villa Igea, Forli, Italy [13]. Donor eyes unsuitable for corneal transplantation due to poor endothelial cell counts, procured by Fondazione Banca degli Occhi del Veneto Onlus (Venice, Italy), were used for research purposes and validation studies described in this manuscript, in accordance with law 91/99 and after an informed consent form was signed by the donor's next of kin. The experimental procedure was approved by the hospital ethics committee (Prot. 2024-0009).

In addition, porcine eyes are utilized in ex vivo tests due to their availability. A key advantage of using ex vivo porcine eyes is the reduced time between exitus and testing. The quality of the cadaver retina significantly declines weeks after exitus, as the lack of blood flow causes the retina to become fragile and detach from underlying layers. Therefore, the lens, vitreous, and detached retina were removed prior to human cadaver eye experiments and left intact for the porcine eye experiments.

For data acquisition, the ex vivo eyes are placed in a holder on the stage, with the trocar aligned to the robot's RCM. To capture a retinal surface of approximately 15×15 mm, the robot executes an automatic grid trajectory that generates approximately 100,000 data points. The ex vivo eye grids are utilized for simulated distance measurements in RViz (Fig. 6), mirroring the data acquisition process in simulation. This method eliminates the necessity for multiple teleoperated scans in ex vivo samples, conserving operating time and minimizing manual segmentation.

D. Modeling parameters identification

First, the optimal parameters for the modeling approaches RBF, OK and B-splines are determined for use in subsequent experiments.

The SciPy library's RBF interpolator is utilized with adjustable parameters, including the kernel, number of neighboring points, and smoothing parameter. The initial evaluation focuses on three kernels — thin plate spline, cubic, and quintic — with the smoothing factor as the only unknown parameter. The challenge lies in selecting smoothing parameters that effectively suppress noise while preserving surface details.

To construct the OK interpolation surface, the toolkit PyKrige is used. Adjustable parameters include the assumed variogram model, its parameters, and the number of lags. From the best-fit variogram model, the parameters nugget, sill and range are determined.

To calculate the B-spline surface function, the library SciPy is used. All parameters, except the smoothing parameter, are maintained at their recommended default settings. A smoothing factor analysis is performed to achieve optimal interpolation for varying noise levels.

E. Evaluation

To evaluate the feasibility of reconstructing the retina from iiOCT data, it is essential to determine whether a robotically executed iiOCT scan can capture the retina's surface features in sufficient detail. To this end, we compare our iiOCT grid scan with a microscope-integrated OCT volume scan, which is recognized for its reliable, high-resolution intraoperative imaging in clinical practice. The meshed iiOCT scan point cloud and the surface of the retina extracted from the OCT volume scan of the porcine eye are shown in Fig. 7. The viewing direction of the iiOCT grid scan is aligned with the depth direction of the microscope-integrated OCT. As illustrated in the image, the grid scan captures all details visible in the volume scan.

However, the OCT volumes cannot be used for quantitative comparisons due to the nonlinear distortion present in extraocular OCT images. These distortions arise from fan scanning, where A-scans are swept across a scan angle to create a B-scan, and from the anterior eye segment [14]. Non-optical imaging modalities like MRI do not suffer from these distortions but lack the desired resolution [36]. In our previous work, we demonstrated that the size of the point clouds reconstructed from iiOCT align with the dimensions of the scanned 3D printed eye shapes, as indicated by the low mean absolute errors [19]. Therefore, iiOCT scanning enables detailed and geometrically correct surface scanning.

For this reason, the iiOCT grid scan serves as reference for assessing the accuracy of local models constructed from teleoperated exploration data (Fig. 8). Unlike previous work [19],

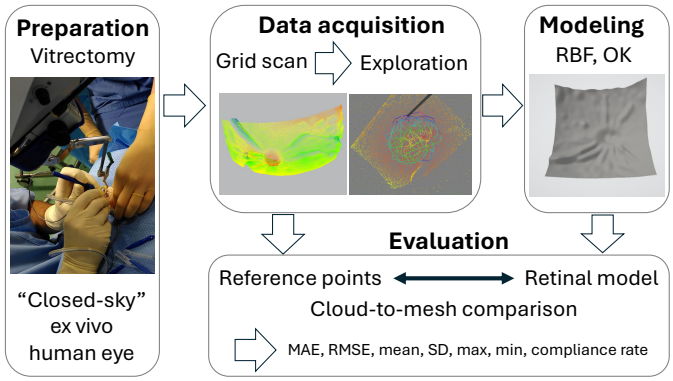

Fig. 8: Evaluation concept: The iiOCT grid scan serves as a reference for assessing the accuracy of the local models. Cloud-to-mesh comparison is performed using CloudCompare

TABLE I: Optimal experimental smoothing factors for RBF and splines, along with the nugget value for OK, for various noise levels ranging from $20\,\mu\text{m}$ to $60\,\mu\text{m}$ added in the instrument direction. Here, x denotes the number of data points divided by 10^3 in the local modeling area

Noise	20 μm	30 μm	40 μm	50 μm	60 μm	Ex vivo
RBF	0.65	1	1.45	2	2.6	0.1
OK	0.022	0.038	0.052	0.066	0.078	0.015
Splines	$0.5x$	x	$1.7x$	$2.6x$	$3.8x$	-

where error was computed against the known geometry of 3D-printed eye shapes, this study requires the ground truth geometry to be obtained from the same sensor, as no other high-precision sensing methods are available. The validity range of the models is defined by the interior of the convex hull around the exploration trajectory. The model surfaces are converted into a fine mesh for cloud-to-mesh comparison with the reference points. This approach reduces evaluation errors compared to point-to-point comparison, as utilized in [19]. The software CloudCompare is used to determine the shortest distance from each reference point to the mesh. From these distances, metrics such as mean absolute error (MAE), root mean square error (RMSE), mean, and standard deviation (SD) are evaluated. Compliance with different maximum errors is assessed by the percentage of distances below the specified threshold ($50\,\mu\text{m}$ and $100\,\mu\text{m}$).

IV. Results

A. Optimal modeling parameters

A radial basis function that is less sensitive to parameter variations is preferred. The quintic kernel exhibits consistent behavior across various smoothing factors. In contrast, kernels like cubic, thin plate spline, and Gaussian, which includes an additional shape parameter ϵ, yield comparable results but necessitate careful tuning, as minor parameter changes can greatly affect quality. The optimal smoothing factor is selected to minimize the mean squared error (MSE). The resulting smoothing factors for different noise levels using the quintic kernel are presented in Table I.

The experimental variograms for the staphyloma eye are illustrated in Fig. 9. The range and sill parameters for different

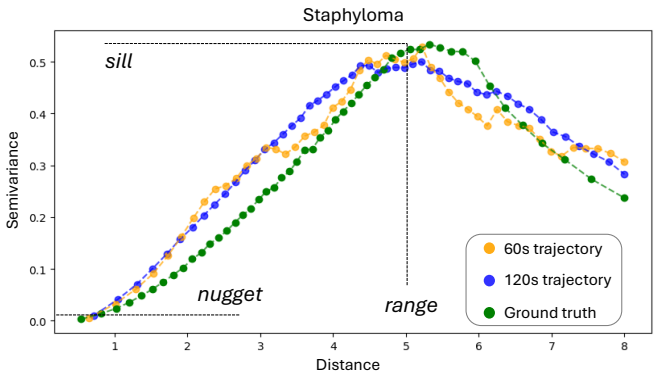

Fig. 9: Experimental variograms for a $60\,\text{s}$ exploration, a $120\,\text{s}$ exploration and the staphyloma ground truth points

TABLE II: Optimal range and sill values for OK interpolation across three eye shapes based on the experimental variograms

	Detachment	Staphyloma	Pointed	Porcine	Human
Range	5.5	4.5	4.5	3.6	4
Sill	0.22	0.5	0.35	0.16	0.08

eye shapes, derived from the experimental variograms, are presented in Table II. However, the nugget value appears underestimated by the experimental variogram, prompting an examination based on the MSE, similar to the RBF smoothing factor selection. A nearly linear relationship between noise and the nugget is observed in Table I.

For splines, the optimal smoothing factor is influenced by the number of data points, exhibiting a linear trend at a given noise level (Table I).

Given that the ex vivo iiOCT grid scans capture fine surface details such as bumps and folds, the model smoothing is slightly decreased compared to the values obtained in simulation (Table I).

B. Simulation results

The performance of the methods as exploration time increases is illustrated in Fig 10a. At an exploration time of $120\,\text{s}$, all three methods achieve a compliance rate ($100\,\mu\text{m}$) of $100\,\%$ and a MAE below $10\,\mu\text{m}$. Fig. 10b demonstrates the impact of increasing noise levels on interpolation accuracy, revealing that the B-spline model experiences the most significant decline in compliance rate.

Table III summarizes the modeling performance across different eye shapes, considering various noise levels and exploration times, with sphere fitting serving as a baseline.

C. Ex vivo results

The iiOCT grid scan of the porcine eye in Fig. 1 reveals details such as retinal folds near the ONH, highlighted in Fig. 11a, along with smaller irregularities like blood vessels and bumps. RBF modeling, with a suitably small smoothing factor, effectively captures these surface details. Fig. 11b illustrates the enhancement in surface detail achieved during a $120\,\text{s}$ exploration over an area of approximately $55\,\text{mm}^2$.

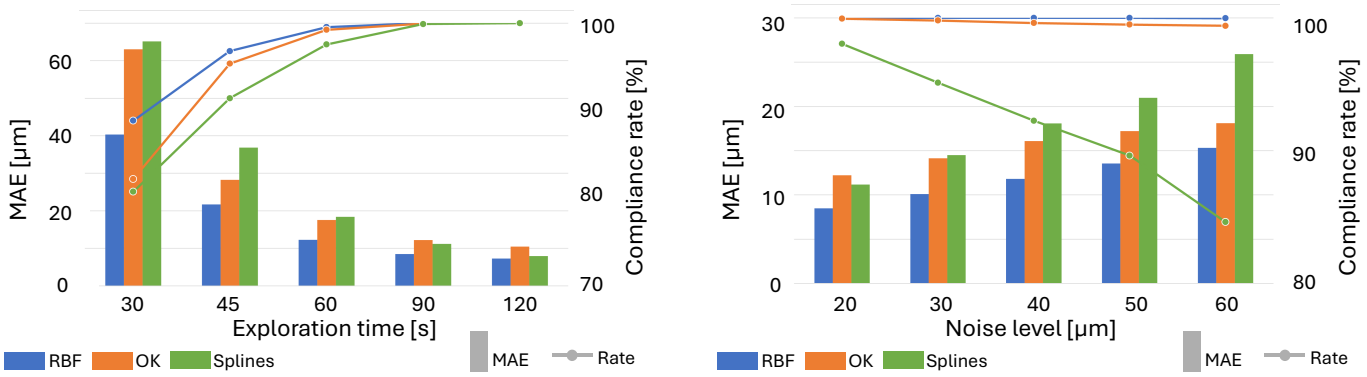

(a) Increasing exploration time (20 µm measurement noise)

(b) Increasing noise level (90 s exploration time)

Fig. 10: Simulation results of RBF, OK, and splines on the retinal detachment eye shape

TABLE III: Simulations results: MAE [µm] of RBF, OK, splines and sphere fitting (SF) for various eye shapes, across different noise levels and exploration times. Bold numerals indicate the most accurate approach

		Retinal detachment				Staphyloma				Pointed retina			
		RBF	OK	Splines	SF	RBF	OK	Splines	SF	RBF	OK	Splines	SF
20 µm	30 s	**40.3**	63.1	65.1	93.4	**24.8**	45.8	50.5	208	13.1	31.9	**12.3**	14.2
	60 s	**12.3**	17.5	18.4	88.5	**8.7**	13.1	17.7	190	**6.3**	9.7	6.6	14.8
	120 s	**7.3**	10.5	8.0	83.7	**7.0**	10.6	11.1	180	8.1	5.2	**4.9**	15.3
50 µm	30 s	**57.3**	71.1	72.1	94.6	43.1	49.6	**33.5**	211	24.7	35.7	**7.0**	11.6
	60 s	**19.3**	25.9	27.8	89.1	13.5	16.9	**9.0**	192	9.6	13.4	**6.8**	12.4
	120 s	**12.2**	17.5	17.6	84.3	10.7	15.7	**9.3**	182	8.8	12.5	**5.6**	13.7

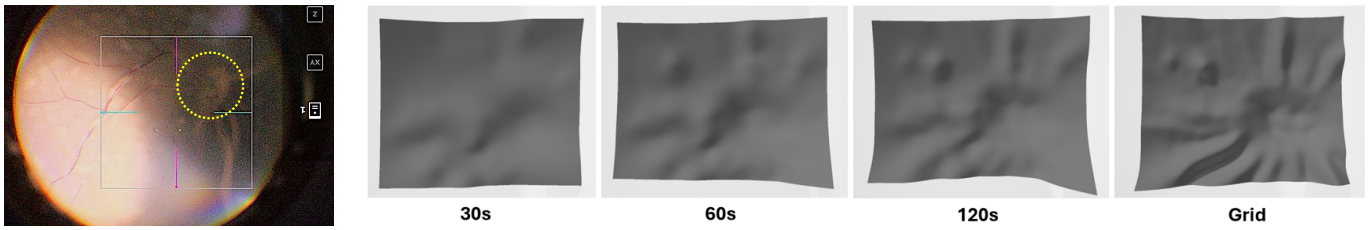

(a) Fundus of a pig

(b) RBF reconstructions with increasing exploration of the porcine eye

Fig. 11: The RBF model progressively reconstructs surface features visible in the fundus image, including the ONH and retinal folds

The area targeted by the endolaser on the human retina prior to the iiOCT grid scan is marked in Fig. 12a. It is important to note that this surface represents the retinal pigment epithelium (RPE), a typically smooth deeper tissue layer. Fig. 12b illustrates the enhancement in surface detail achieved during a 120 s exploration of the human retina. This aims to evaluate how effectively surface details can be derived from a teleoperated, ideally brief, exploration.

Fig. 13 illustrates the improvement in local modeling accuracy as exploration time increases. A comparison of the two modeling methods reveals that RBF is more accurate than OK with fewer data points. Table IV provides a comprehensive overview of the achieved ex vivo results on the grid scan. On the human eye, the OK method achieves an MAE of 21.4 µm and an RMSE of 38.1 µm, compared to an MAE of 75.8 µm and an RMSE of 125 µm for the sphere fit.

The distribution of the shortest cloud-to-mesh distances for OK is illustrated in Fig. 14a. The majority of points lie within 50 µm of the surface, with only a few exceeding 100 µm, primarily located in areas of pronounced retinal folds. Fig. 14b displays the uncertainty heat maps for three exploration du-

TABLE IV: Ex vivo results: MAE, RMSE, mean, SD, maximum and minimum error for RBF, OK, and sphere fitting (SF), along with their compliance rates (CR). Bold numerals indicate the most accurate approach

	Porcine eye			Human eye		
	RBF	OK	SF	RBF	OK	SF
MAE [µm]	26.5	**14.7**	198	25.5	**21.4**	75.8
RMSE [µm]	44.4	**19.6**	270	43.8	**38.1**	125
Mean [µm]	**-0.05**	-2.7	-3.4	1.64	-2.11	**-0.54**
SD [µm]	44.4	**19.6**	270	43.7	**38**	125
Max [µm]	280	**128**	823	**287**	298	491
Min [µm]	-408	**-170**	-1400	**-437**	-452	-841
$CR_{100\,\mu m}$ [%]	95.1	**99.7**	31.7	95.4	**96.5**	81.8
$CR_{50\,\mu m}$ [%]	85.6	**98.3**	15.3	86.8	**90**	50.2

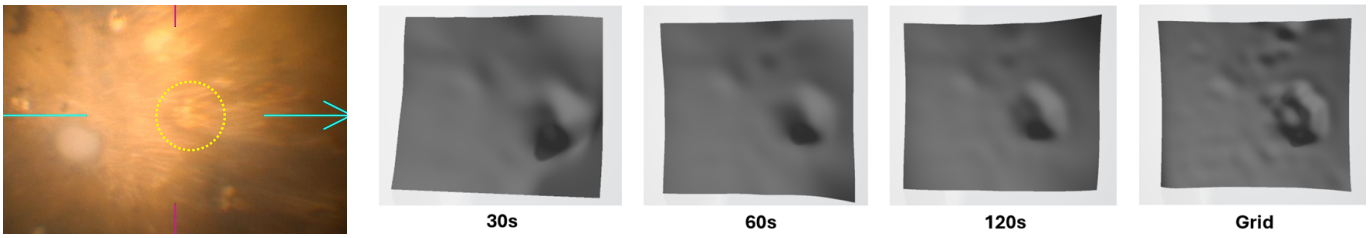

(a) Fundus of a human (b) RBF reconstructions with increasing exploration of the human eye

Fig. 12: The RBF model progressively reconstructs surface features visible in the fundus image, including the endolaser target point

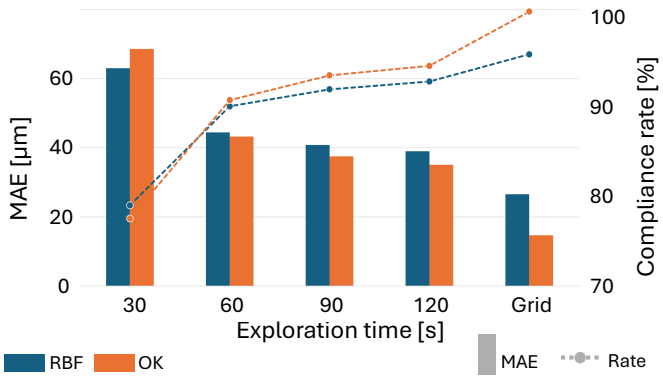

Fig. 13: MAE and compliance rate improvement with increasing exploration time on a porcine ex vivo eye

rations, along with the reference point clouds color-coded by MAE, where green coloration indicates absolute distances close to zero. Gaps in the point cloud indicate that the surface accuracy does not meet the requirement. The gaps close with increased exploration, while the OK variance decreases.

The computation time on a CPU (Intel Core i5-1245U, 1.60 GHz, 16 GB RAM) to construct the local models based on a $120\,\mathrm{s}$ exploration is $6.9\,\mathrm{ms}$ for B-splines, $0.9\,\mathrm{s}$ for RBF and $8.7\,\mathrm{s}$ for OK.

V. Discussion

A. Simulation results

RBF modeling excels with sparse, non-uniform datasets and, when using an appropriate smoothing factor, mitigates overfitting. It effectively handles noise up to $60\,\mu\mathrm{m}$, ensuring reliable surface representation across various eye shapes. The $100\,\%$ compliance rate for all eye shapes after $90\,\mathrm{s}$ underscores the significance of thorough exploration.

Comparison of OK variograms with exploration and ground truth data shows that the statistical structure can be estimated within $1\,\mathrm{min}$. In contrast, RBF interpolation uses a fixed kernel that is not customized for the data. Given their comparable accuracy, it is essential to acknowledge their close algebraic link as shown by Scheuerer et al. [30].

The strong performance of B-splines for regular surfaces, such as the pointed retina, highlights their suitability in simulation. As a local interpolation method, they effectively handle large datasets, as updates to a model only impact a small surface area. This reduces computational effort and eliminates the need to invert large covariance matrices, as required by OK. However, this advantage comes with edge instabilities and oscillations. Additionally, the precise and error-prone tuning of the smoothing parameter, influenced by noise and data quantity, hampers further investigations.

B. Ex vivo results

The resolution of the RBF surfaces significantly improves with exploration time. After $2\,\mathrm{min}$, all details visible on the grid scan-based model are discernible. However, the methods struggle to accurately represent the surface in areas with overlapping retinal folds. The distance histogram reveals that these outliers constitute a minor portion of the total cloud, with most reference points within $50\,\mu\mathrm{m}$ of the model. These pronounced retinal detachments in ex vivo eyes arise from rapid post-slaughter degeneration. Less severe detachments are anticipated in human in vivo eyes.

For both RBF and OK, the MAE drops below $40\,\mu\mathrm{m}$ after $120\,\mathrm{s}$, achieving a compliance rate exceeding $90\,\%$. This is benchmarked against the accuracy achievable when modeling the dense iiOCT grid scan, which is approximately $20\,\mu\mathrm{m}$. The accuracy difference between our models and the state-of-the-art sphere fitting is evident, as the sphere fit averages many surface details to capture global geometry, whereas the the local methods aim to approximate these details.

For the intra-ocular trajectories, the OK variance of the examined area is represented as a heat map. The color-coded point clouds show that most modeling inaccuracies occur in areas with higher OK variance. This observation suggests that variance information could offer insights into the surface exploration required for a reliable model.

None of the methods can filter or disregard outliers. In real-world distance measurements with an iiOCT fiber, errors may arise from factors such as blood or detached tissue fragments [37]. Thus, stable and robust distance measurement, followed by data filtering, is crucial before modeling. Additionally, while the models can perform interpolation, they are unsuitable for extrapolation.

In conclusion, our proposed methods successfully model complex micro-anatomical surfaces. Future work will focus on integrating these models into the Geyedance robotic platform to provide model-based assistance, including virtual boundaries [13], thereby improving safety in delicate ophthalmic procedures.

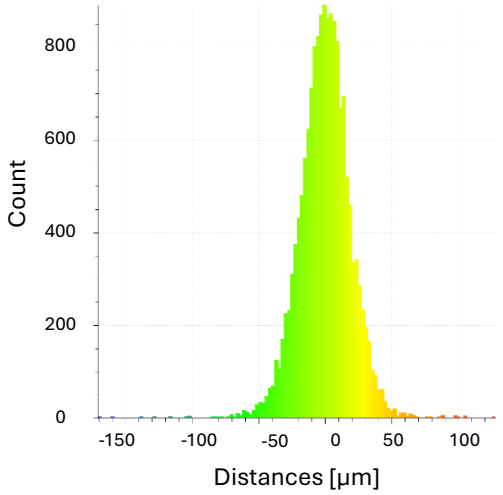

(a) Histogram of the shortest distances from the grid point cloud to the corresponding surface model

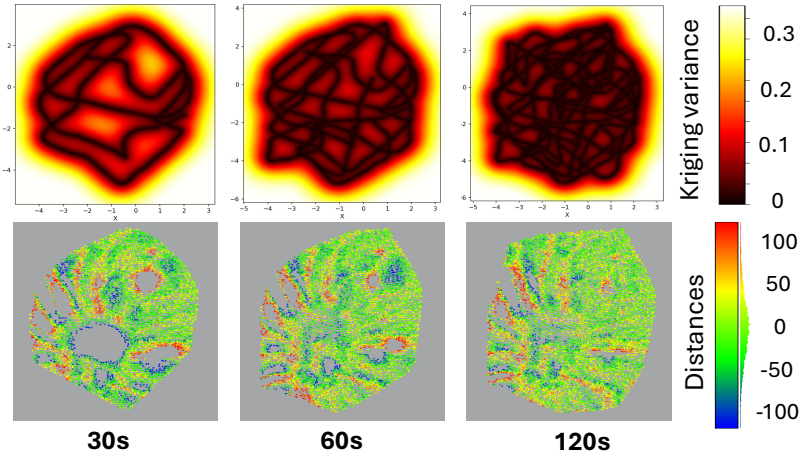

(b) OK variance heat maps for the 30 s, 60 s, and 120 s exploration, along with the color-coded grid point cloud, showing only the points with absolute distances below 100 µm

Fig. 14: OK surface fitting results on the porcine eye

C. In vivo movements

One factor affecting the precision of in vivo iiOCT-based surface reconstruction is patient head movements, including involuntary retinal movements [38]. Despite general anesthesia, the eye moves in response to respiration and heartbeat. Cereda et al. analyzed the in vivo iiOCT data from a static sensor in five patients, revealing repetitive movements patterns with amplitudes of approximately 10 µm for heartbeat and 20 µm for breathing [6]. Notably, one snoring patient exhibited an amplitude of 100 µm. In a related study, McCannel et al. found that during 37 procedures under local anesthesia with snoring, 18 patients suddenly moved their heads, compared to only 1 % of procedures without snoring [39]. While models can compensate for predictable quasi-periodic movements [40], unexpected non-periodic movements, such as skipped heartbeats or sudden snoring-related movements, pose greater challenges for compensation. Additionally, our pre-surgery modeling approach does not account for intraoperative tissue changes.

VI. Conclusion

In conclusion, this research effectively integrates fiber-based distance sensing with instrument tracking for precise surface reconstruction in eye surgery. Our findings demonstrate that the proposed methods are well-suited for modeling non-uniform point clouds, with RBF interpolation demonstrating superior stability and accuracy in both simulations and ex vivo data. This work does not address in vivo movements, such as involuntary eye motions from heartbeat and breathing, which remain significant challenges and will be addressed in future work. While periodic movements can be modeled, unexpected motions complicate compensation. The significance of this research lies in its potential to enhance intraoperative feedback modalities, facilitating more precise instrument manipulation.

References

[1] E. Z. Ahronovich, N. Simaan, and K. Joos, "A review of robotic and OCT-aided systems for vitreoretinal surgery," *Advances in Therapy*, vol. 38, pp. 2114–2129, 2021. DOI: 10.1007/s12325-021-01692-z.

[2] X. Li, C. Chudoba, T. Ko, C. Pitris, and J. G. Fujimoto, "Imaging needle for optical coherence tomography," *Optics Letters*, vol. 25, no. 20, pp. 1520–1522, 2000. DOI: 10.1364/OL.25.001520.

[3] C. Song, D. Y. Park, P. L. Gehlbach, S. J. Park, and J. U. Kang, "Fiber-optic OCT sensor guided "SMART" micro-forceps for microsurgery," *Biomedical Optics Express*, vol. 4, no. 7, pp. 1045–1050, 2013. DOI: 10.1364/BOE.4.001045.

[4] A. Abid, R. Duval, F. Rezende, and C. Boutopoulos, "A smart vitrector equipped by a fiber-based OCT sensor mitigates intentional attempts at creating iatrogenic retinal breaks during vitrectomy in pigs," *Translational Vision Science & Technology*, vol. 10, no. 13, p. 19, 2021. DOI: 10.1167/tvst.10.13.19.

[5] H. Ramakonar, B. C. Quirk, R. W. Kirk, *et al.*, "Intraoperative detection of blood vessels with an imaging needle during neurosurgery in humans," *Science Advances*, vol. 4, no. 12, 2018. DOI: 10.1126/sciadv.aav4992.

[6] M. G. Cereda, S. Parrulli, Y. Douven, *et al.*, "Clinical evaluation of an instrument-integrated OCT-based distance sensor for robotic vitreoretinal surgery," *Ophthalmology Science*, vol. 1, no. 4, 2021. DOI: 10.1016/j.xops.2021.100085.

[7] M. Zhou, J. Wu, A. Ebrahimi, *et al.*, "Spotlight-based 3D instrument guidance for retinal surgery," in *2020 International Symposium on Medical Robotics (ISMR)*, 2020, pp. 69–75. DOI: 10.1109/ISMR48331.2020.9312952.

[8] H. A. Madi and J. Keller, "Increasing frequency of hospital admissions for retinal detachment and vitreo-

retinal surgery in england 2000–2018," *Eye*, vol. 36, pp. 1610–1614, 2022. DOI: 10.1038/s41433-021-01647-2.

[9] M. Sommersperger, J. Weiss, M. A. Nasseri, P. Gehlbach, I. Iordachita, and N. Navab, "Real-time tool to layer distance estimation for robotic subretinal injection using intraoperative 4D OCT," *Biomedical Optics Express*, vol. 12, no. 2, pp. 1085–1104, 2021. DOI: 10.1364/BOE.415477.

[10] P. Xu, M. Ourak, G. Borghesan, and E. Vander Poorten, "Fast OCT-based needle tracking for retinal microsurgery using dynamic spiral scanning," *IEEE Transactions on Medical Robotics and Bionics*, vol. 6, no. 4, pp. 1502–1511, 2024. DOI: 10.1109/TMRB.2024.3464693.

[11] J. W. Kim, S. Wei, P. Zhang, *et al.*, "Towards autonomous retinal microsurgery using RGB-D images," *IEEE Robotics and Automation Letters*, vol. 9, no. 4, pp. 3807–3814, 2024. DOI: 10.1109/LRA.2024.3368192.

[12] M. A. Nasseri, M. Eder, D. Eberts, *et al.*, "Kinematics and dynamics analysis of a hybrid parallel-serial micromanipulator designed for biomedical applications," in *2013 IEEE/ASME International Conference on Advanced Intelligent Mechatronics*, 2013, pp. 293–299. DOI: 10.1109/AIM.2013.6584107.

[13] N. Piccinelli, L. Haide, M. Briel, *et al.*, "GEYEDANCE: An OCT-enhanced multi-modal feedback platform for robot-assisted ophthalmic surgery," *IEEE Transactions on Medical Robotics and Bionics*, 2025. DOI: 10.1109/TMRB.2025.3583133.

[14] R. Grytz, M. E. Hamdaoui, P. A. Fuchs, *et al.*, "Nonlinear distortion correction for posterior eye segment optical coherence tomography with application to tree shrews," *Biomedical Optics Express*, vol. 13, no. 2, pp. 1070–1086, 2022. DOI: 10.1364/BOE.447595.

[15] T. Probst, K.-K. Maninis, A. Chhatkuli, M. Ourak, E. Vander Poorten, and L. Van Gool, "Automatic tool landmark detection for stereo vision in robot-assisted retinal surgery," *IEEE Robotics and Automation Letters*, vol. 3, no. 1, pp. 612–619, 2018. DOI: 10.1109/LRA.2017.2778020.

[16] R. Peter, S. Moreira, E. Tagliabue, M. Hillenbrand, R. G. Nunes, and F. Mathis-Ullrich, "Stereo reconstruction from microscopic images for computer-assisted ophthalmic surgery," *International Journal of Computer-Assisted Radiology and Surgery*, vol. 20, no. 3, pp. 605–612, 2025. DOI: 10.1007/s11548-024-03177-0.

[17] P. Cornelissen, M. Ourak, G. Borghesan, D. Reynaerts, and E. Vander Poorten, "Towards real-time estimation of a spherical eye model based on a single fiber OCT," in *19th International Conference on Advanced Robotics (ICAR)*, 2019, pp. 666–672. DOI: 10.1109/ICAR46387.2019.8981620.

[18] D. Zhou, H. Takeyama, S. Nakao, K.-H. Sonoda, and K. Tadano, "Real-time fundus reconstruction and intraocular mapping using an ophthalmic endoscope," *The International Journal of Medical Robotics and Computer Assisted Surgery*, vol. 19, no. 3, 2023. DOI: 10.1002/rcs.2496.

[19] M. Briel, L. Haide, M. Hess, *et al.*, "Intraoperative adaptive eye model based on instrument-integrated OCT for robot-assisted vitreoretinal surgery," *International Journal of Computer-Assisted Radiology and Surgery*, 2025. DOI: 10.1007/s11548-025-03325-0.

[20] M. Briel, L. Haide, M. Meyling, *et al.*, "Curvature-corrected retinal registration of diagnostic OCT with instrument-integrated OCT," *Manuscript submitted for publication*, 2025.

[21] R. Franke, "Scattered data interpolation: Tests of some methods," *Mathematics of Computation*, vol. 38, no. 157, 1982. DOI: 10.2307/2007474.

[22] M. A. Oliver and R. Webster, "Kriging: A method of interpolation for geographical information systems," *International Journal of Geographical Information Systems*, vol. 4, no. 3, pp. 313–332, 1990. DOI: 10.1080/02693799008941549.

[23] S. Moon and K. Ko, "A point projection approach for improving the accuracy of the multilevel B-spline approximation," *Journal of Computational Design and Engineering*, vol. 5, no. 2, pp. 173–179, 2018. DOI: 10.1016/j.jcde.2017.10.004.

[24] J. Carr, W. Fright, and R. Beatson, "Surface interpolation with radial basis functions for medical imaging," *IEEE Transactions on Medical Imaging*, vol. 16, no. 1, pp. 96–107, 1997. DOI: 10.1109/42.552059.

[25] M. R. Stytz and R. W. Parrott, "Using kriging for 3D medical imaging," *Computerized Medical Imaging and Graphics*, vol. 17, no. 6, pp. 421–442, 1993. DOI: 10.1016/0895-6111(93)90059-V.

[26] S. Lee and J. U. Kang, "CNN-based CP-OCT sensor integrated with a subretinal injector for retinal boundary tracking and injection guidance," *Journal of Biomedical Optics*, vol. 26, no. 6, 2021. DOI: 10.1117/1.JBO.26.6.068001.

[27] D. E. Myers, "Smoothing and interpolation with radial basis functions," *WIT Transactions on Modelling and Simulation*, vol. 23, 1999. DOI: 10.2495/BT990341.

[28] M. Hillier, "Radial basis functions," in *Encyclopedia of Mathematical Geosciences*. 2021. DOI: 10.1007/978-3-030-26050-7_263-1.

[29] I. Raid, T. Kusnezowa, and J. Seewig, "Application of ordinary kriging for interpolation of micro-structured technical surfaces," *Measurement Science and Technology*, vol. 24, no. 9, 2013. DOI: 10.1088/0957-0233/24/9/095201.

[30] M. Scheuerer, R. Schaback, and M. Schlather, "Interpolation of spatial data – a stochastic or a deterministic problem?" *European Journal of Applied Mathematics*, vol. 24, no. 4, pp. 601–629, 2013. DOI: 10.1017/S0956792513000016.

[31] M. Dewan, P. Marayong, A. Okamura, and G. Hager, "Vision-based assistance for ophthalmic micro-surgery," in *Medical Image Computing and Computer-Assisted*

Intervention – MICCAI 2004, vol. 3217, 2004, pp. 49–57. DOI: 10.1007/978-3-540-30136-3_7.

[32] P. H. C. Eilers and B. D. Marx, "Flexible smoothing with B-splines and penalties," *Statistical Science*, vol. 11, no. 2, pp. 89–121, 1996. DOI: 10.1214/ss/1038425655.

[33] N. Nakao, T. Igarashi-Yokoi, H. Takahashi, S. Xie, K. Shinohara, and K. Ohno-Matsui, "Quantitative evaluations of posterior staphylomas in highly myopic eyes by ultra-widefield optical coherence tomography," *Investigative Ophthalmology & Visual Science*, vol. 63, no. 8, pp. 20–20, 2022. DOI: 10.1167/iovs.63.8.20.

[34] T. Iwase, R. Tomita, E. Ra, C. Iwase, and H. Terasaki, "Investigation of causative factors for unusual shape of macula in eyes with macula-off rhegmatogenous retinal detachment," *Japanese Journal of Ophthalmology*, vol. 65, pp. 363–371, 2021. DOI: 10.1007/s10384-020-00810-8.

[35] M. Moriyama, K. Ohno-Matsui, T. Modegi, *et al.*, "Quantitative analyses of high-resolution 3D MR images of highly myopic eyes to determine their shapes," *Investigative Ophthalmology & Visual Science*, vol. 53, no. 8, pp. 4510–4518, 2012. DOI: 10.1167/iovs.12-9426.

[36] L. van Vught, D. P. Shamonin, G. P. M. Luyten, B. C. Stoel, and J.-W. M. Beenakker, "MRI-based 3D retinal shape determination," *BMJ Open Ophthalmology*, vol. 6, no. 1, 2021. DOI: 10.1136/bmjophth-2021-000855.

[37] M. Briel, L. Haide, T. Weber, *et al.*, "Intraoperative fusion of models and data for robust distance sensing," *Manuscript submitted for publication*, 2025.

[38] R. de Kinkelder, J. Kalkman, D. J. Faber, *et al.*, "Heartbeat-induced axial motion artifacts in optical coherence tomography measurements of the retina," *Investigative Ophthalmology & Visual Science*, vol. 52, no. 6, pp. 3908–3913, 2011. DOI: 10.1167/iovs.10-6738.

[39] C. A. McCannel, E. J. Olson, M. J. Donaldson, S. J. Bakri, J. S. Pulido, and D. Mueller, "Snoring is associated with unexpected patient head movement during monitored anesthesia care vitreoretinal surgery," *Retina*, vol. 32, no. 7, pp. 1324–1327, 2012. DOI: 10.1097/IAE.0b013e31823bea54.

[40] C. Riviere, J. Gangloff, and M. De Mathelin, "Robotic compensation of biological motion to enhance surgical accuracy," *Proceedings of the IEEE*, vol. 94, no. 9, pp. 1705–1716, 2006. DOI: 10.1109/JPROC.2006.880722.